Acta Astronautica 231 (2025) 47–63

Contents lists available at ScienceDirect

Acta Astronautica

journal homepage: www.elsevier.com/locate/actaastro

Research paper

Preliminary analysis and design of an optical space surveillance and tracking constellation for LEO coverage

A. D'Anniballe *, L. Felicetti, S. Hobbs

Cranfield University, College Road, Cranfield, MK43 0AL, United Kingdom

ARTICLE INFO

Keywords:
Space surveillance
Constellation design
Space debris
Orbit determination

ABSTRACT

Accurately tracking space debris and operational satellites is the foundation of the long-term sustainability of space operations. To improve upon some of the inherent limitations of ground radars, a constellation of satellites carrying optical sensors for the surveillance of the Low Earth Orbit (LEO) region is analysed. This analysis aims to understand the performance drivers of such a system in terms of constellation geometry and provide a general methodology for the preliminary design of the system. First, a method for decoupling the design of the optical payload and the constellation geometry while retaining statistically significant results is shown. Using the resulting estimate for the maximum observable distance, an approximate method for computing the coverage of the system is proposed. The expected daily and yearly variation of coverage depending on its own dynamics and the position of the Sun is analysed, showing that it has a small impact on the design process. The dependence of the coverage on constellation parameters such as altitude, inclination and distribution of satellites is investigated through parametric analysis, retrieving an estimate for the Pareto front of the system. Building upon the previous results, a random search method is shown to be effective in finding a design point lying on the Pareto front that is robust to both random satellite loss and deployment strategy. Finally, a reduced budget architecture is proposed to achieve acceptable performance while using only a few tens of satellites. The resulting work answers the problems of estimating and optimising the performance of a distributed system for space-based surveillance of the LEO region, a stepping stone for future cost–benefit analyses for the enhancement of space surveillance networks.

1. Introduction

The near-Earth space is getting crowded. The number of anthropogenic objects has more than doubled in the past ten years, with a tenfold increase in payloads in the Low Earth Orbit (LEO) region alone [1]. Such trends are unlikely to reverse soon. In the coming years, SpaceX plans to more than double its current fleet of 5000 satellites for broadband internet [2]. Similar systems are currently being explored by Amazon with the proposed Kuiper constellation [3] and by China with the Guowang project [4]. Even though any operator can in principle safely operate its own fleet, the lack of agreed guidelines and common space traffic coordination frameworks raises the risk of collision between spacecraft operated by different entities, causing mission failures and generating debris. Indeed, a few events in recent times like the ASAT test involving Fengyun-1C [5] and the 2009 Cosmos-Iridium collision [6] generated a large amount of debris, and ESA forecasts a steady increase in the number of catastrophic collisions per year at the current conditions [1].

To avoid collisions, it is paramount to predict close approach events and therefore to accurately know in real time the position and velocity of as many of those potentially dangerous objects that are theoretically trackable. Systems providing this service are known as Space Surveillance and Tracking (SST) systems. SST service providers observe the sky and track specific objects by means of networks of radar and optical sensors. By processing their measurements, they are able to regularly update a catalogue of space objects and promptly communicate any anomaly or conjunction event to satellite operators. Examples of SST service providers are the US SSN [7], the European EU SST [8], international collaborations such as ISON [9], and private companies such as LeoLabs [10].

Most of these providers rely on ground networks of sensors, with radar systems usually dedicated to LEO object tracking and optical telescopes for the Geostationary (GEO) region and beyond. Due to the distribution of land on Earth and the difficulties in establishing agreements between different countries, the resulting network coverage can be uneven. For instance, the radar sensors of the US SSN are

* Corresponding author.
E-mail address: antonio.danniballe@cranfield.ac.uk (A. D'Anniballe).

https://doi.org/10.1016/j.actaastro.2025.02.019
Received 11 November 2024; Received in revised form 22 January 2025; Accepted 12 February 2025
Available online 21 February 2025
0094-5765/© 2025 The Authors. Published by Elsevier Ltd on behalf of IAA. This is an open access article under the CC BY license (http://creativecommons.org/licenses/by/4.0/).

concentrated in the western part of Earth's northern hemisphere. A possible solution is to move sensors to space, providing a scalable system to reach even continuous coverage. Optical sensors are ideal for space-based sensing, as they can provide angular position data with accuracy in the order of a few arcseconds with low power consumption compared to radar systems [11]. The US SSN currently employs space-based surveillance by means of the Canadian satellite Sapphire [12] and the SBSS system [13]. Both of these systems use optical sensors as measurement devices, but they are designed to target the GEO region.

LEO objects are indeed harder to track from space: they are shadowed for a greater portion of their orbits and fly at a higher speed compared to GEO. An object that is being shadowed does not reflect visible light, while one that goes too fast cannot be effectively captured within the camera shutter time. To compensate for these issues and provide continuous coverage, we can use a constellation of small, inexpensive satellites carrying less expensive optical sensors. To compensate for the tracking issues in the LEO region, instead of a single satellite only capable of covering a specific portion of the sky, a network of distributed sensors could be employed. A natural example of an optical sensor network is a constellation of small satellites carrying telescopes. A complete analysis of such a system would require the preliminary design of the optical instrument, the definition of the tracking strategy and the specification of the constellation geometry maximising some definitions of coverage.

Past research already addresses some aspects of the system analysis. Rider was the first to analyse the concept for Above-The-Horizon (ATH) coverage and generic sensor, providing analytical estimates on the number of satellites needed for full coverage [14,15], while recent work by Hussain et al. explored the possibility of a distributed satellite architecture for Space-Based Space Surveillance using dual-use star trackers [16]. To analyse the system performance as a function of the constellation parameters, we need a method for computing the coverage of the constellation: Biria et al. derived an analytical method for coverage computation in the 2D case [17] and Takano et al. used it to find the optimal parameters of the constellation [18]. Another approach was the one carried on by Sun et al. who developed an efficient ring-based discretisation method for computing the total coverage [19]. In both cases the analysed system employed generic sensors, neglecting the impact of lighting on the visibility of the target object when using an optical payload. A preliminary performance analysis accounting for such visibility conditions was performed by D'Anniballe et al. who showed that three optical space-based measurements are enough to accurately track a given LEO target using an Unscented Kalman Filter, a result that will be used in this work for defining coverage [20]. A preliminary analysis aimed at finding suitable optical instruments for space-based optical surveillance compatible with the use of CubeSats was performed by Pineau et al. who found possible candidates among available off-the-shelf camera lenses, and whose results will be used in this work for estimating the expected maximum range of the observations [21].

In this paper, we extend past research by showing a possible way of decoupling the problems of instrument and constellation design, while proposing a new method for coverage estimation accounting for the lighting conditions of the target object. First, we obtain semi-analytical estimates for the maximum observation range when using optical sensors similar to available off-the-shelf cameras. Then, we analyse the constellation coverage as a function of the constellation parameters, together with its yearly variation due to the periodic motion of the Sun with respect to the Earth. After proposing a Monte Carlo integration scheme for coverage estimation, we perform a parametric analysis to retrieve the dependence of the coverage on the constellation parameters in the three-dimensional case under the assumption of a Walker-like architecture. After estimating the Pareto front of the system, we show that random search is a quick method of reaching an optimal solution, and an optimal design point is consequently chosen. We conclude with a robustness analysis of the system, a comparison of potential launch and deployment strategies, and a proposal for a reduced-budget architecture that retains good performance. The resulting paper answers the problems of estimating and optimising the performance of a distributed system for space-based space surveillance in LEO and is therefore a stepping stone in including such systems in future cost–benefit analyses for the enhancement of space surveillance networks.

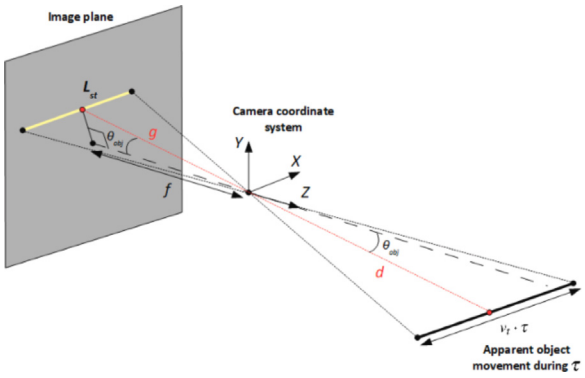


Fig. 1. Pinhole camera model [21].

2. Optical sensor analysis

In this section, we retrieve an estimate for the maximum range of the observing cameras of the constellation, i.e. the maximum distance from the observer at which a given target is visible. First, we build a model for the camera and the Signal-to-Noise ratio of a measurement, which will depend on the target velocity. Then, we retrieve some analytical estimates for the distribution of the target velocities. Aiming to observe at least 50% of targets of 10 cm size, we finally compute the maximum range.

2.1. Camera model and signal-to-noise ratio

We use a pinhole camera model for the optical sensor as shown in Fig. 1.

The model assumes the camera is a lens projecting a target object on a screen through single-point focusing. The main parameters of the optical sensor are then the focal length f, the aperture D, the sensor dimensions b_1 (width) and b_2 (height). These numbers define a focal ratio $F = f/D$ and a rectangular field of view with aperture angles $\Phi_k = 2\arctan\frac{b_k}{2f}$, $k = 1,2$. In this work, we assume a square field of view with $\Phi_1 = \Phi_2 = \Phi$. We assume we capture the image of the target with an electro-optical device like a CCD- or CMOS-based camera. When a photon hits a pixel of the image frame, it is converted into an electric charge by a photosensor. The electrons thus generated produce the current at a given time. The integration of the current over the time in which the camera shutter is open, also known as the exposure or shutter time, constitutes the input base for the image formation. This input, however, is not composed only by the light reflected by the desired target, but also by other noise sources. The main performance parameter in sensor selection is therefore the ratio between the meaningful input and the meaningless input, also called the Signal-to-Noise Ratio (SNR). This ratio is equivalent to the mean power of the signal over the mean power of the noise. We use the model developed by Pineau et al. for the computation of the SNR [21]. The model assumes the target to be a square plate of side length r using an isotropic model for the diffuse reflection neglecting the light reflected from the borders of the plate. The computed signal is then:

$$S = Q\frac{P_c\tau}{h\nu} \tag{1}$$

with Q quantum efficiency (i.e. the average number of electrons generated per incoming photon), h Planck's constant, ν photon frequency,

Table 1
Electro-optical and noise parameters [21].

Symbol	Parameter	Value	Unit
f	Focal length	0.4	m
F	Focal ratio	2.8	–
Φ	Field of view	5	°
Q	Quantum efficiency	61	%
τ	Shutter time	0.025	s
p	Pixel size	12	μm
K	Sky count rate per pixel	0.01	e^- s^{-1} pixel^{-1}
I_{dark}	Dark current	0.03	e^- s^{-1} pixel^{-1}
R_N	Readout noise	4.3	e^- pixel^{-1}

and P_c power received by the camera. This is computed as:

$$P_c = 0.4\frac{\rho H r^2 D^2}{8d^2} \tag{2}$$

with $H = 1361$ Wm^{-2} solar constant, ρ target reflectance, d target–observer distance. We assume $\rho = 0.3$ [22]. To model the visible spectrum, we use the approximate peak value $\nu = 600$ THz. The model assumes the noise to be the sum of four independent random noises:

- *Target shot noise* (σ_{shot}): noise due to the discrete nature of the electric charge, modelled as a Poisson process, associated to the photons reflected by the target.
- *Sky noise* (σ_{sky}): shot noise associated to the incoming photons not belonging to the target.
- *Dark noise* (σ_{dark}): electrons randomly generated in the depletion region of the detector.
- *Readout noise* (σ_R): noise introduced by the signal amplification.

The total noise, assumed to be Gaussian, is then:

$$N = \sqrt{\sigma_{shot}^2 + \sigma_{sky}^2 + \sigma_{dark}^2 + \sigma_R^2} \tag{3}$$

with:

$$\sigma_{shot}^2 = S \tag{4}$$

$$\sigma_{sky}^2 = K n_{ip} \tau \tag{5}$$

$$\sigma_{dark}^2 = I_{dark} n_{ip} \tau \tag{6}$$

$$\sigma_R^2 = R_N^2 n_{ip} \tag{7}$$

where K is the sky count rate per pixel, I_{dark} is the dark current of the sensor, R_N is the readout noise of the sensor, n_{ip} is the number of the illuminated pixels. This last quantity is the result of the path that the target object traces on the field of view, also known as streak, and can be approximated as:

$$n_{ip} = L_{st} W_{st} \tag{8}$$

where L_{st} is the approximate streak length and W_{st} is the approximate streak width. Pineau et al. prove that:

$$n_{ip} = 2.44\frac{\upsilon_T \tau f^2}{d D p^2 \cos\theta_{obj}} \tag{9}$$

where υ_T is the target averaged tangential velocity relative to the sensor, d is the distance between the target and the sensor, p is the pixel size, θ_{obj} is the angle between the line of sight of the camera and the direction of the object as seen from the centre of the camera coordinate system. The electro-optical and noise parameters for the sensing system used in this work are summarised in Table 1.

The signal-to-noise ratio will then be:

$$SNR = S/N \tag{10}$$

and will depend on the target parameters summarised in Table 2. The target parameters are only three because, owing to the small angular aperture $\Phi = 5°$, we can assume $\theta_{obj} = 0°$. The signal will be accepted whenever it will be five times the noise, or $SNR > 5$. A different way to look at the problem is by considering the apparent magnitude of the target object. A target that is far away will appear less bright than a nearby target, and therefore will require an higher exposure time to produce the same signal. Once the exposure, or shutter time, τ is fixed, the signal-to-noise ratio will be a monotonic function of the apparent magnitude. Fixing the minimum signal-to-noise ratio to 5, one can find the corresponding limiting magnitude of the sensor. To show the results for the sensor parameters in Table 1, with τ fixed to 0.025 s, we use a Monte Carlo simulation initialising 500 random targets and the apparent magnitude model found in Clemens (2019) [23]. The results are shown in Fig. 2, where the limiting magnitude can be retrieved as approximately equal to 12.

Table 2
Target parameters.

Symbol	Parameter	Unit
r	Target size	m
d	Target distance	m
υ_T	Tangential velocity relative to sensor	m s^{-1}

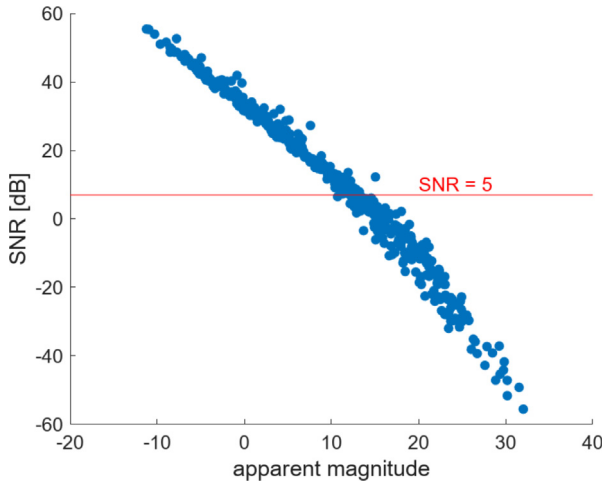


Fig. 2. Signal-to-noise ratio against apparent magnitude for the sensor parameters in Table 1. The curve is retrieved using a Monte Carlo simulation with random target parameters. The resulting limiting magnitude is approximately 12.

2.2. Maximum observable range

A target which is too small or too distant will be too faint to be observable. Moreover, if the target–observer relative velocity is too high, most of the reflected photons will distribute over a long streak, lowering the signal per pixel. A high relative velocity may also mean that the target is not captured at all by the camera, as it passes the field of view in a time lower than the shutter time τ. This allows us to define the minimum observable distance as:

$$d_{min} = 2\frac{\upsilon_T \tau}{\tan(\Phi/2)} \tag{11}$$

The worst scenario is the case where the target and the observer fly in opposite directions, in which case υ_T is 15.3 km/s (two times the orbital velocity at an altitude of 400 km), resulting in $d_{min} = 17.5$ km. This distance is very small and will contribute little to the loss of coverage, allowing us to discard it during the coverage estimation process. We define the maximum observable range instead to be the maximum distance at which it would be theoretically possible to observe at least 50% of targets of size above 10 cm with the given instrument. The size of 10 cm is chosen because the space-based surveillance system focuses on all the objects that are virtually certain to cause critical failures in case of collision. Since the target size is set, and the maximum observable distance is an unknown quantity, the only independent

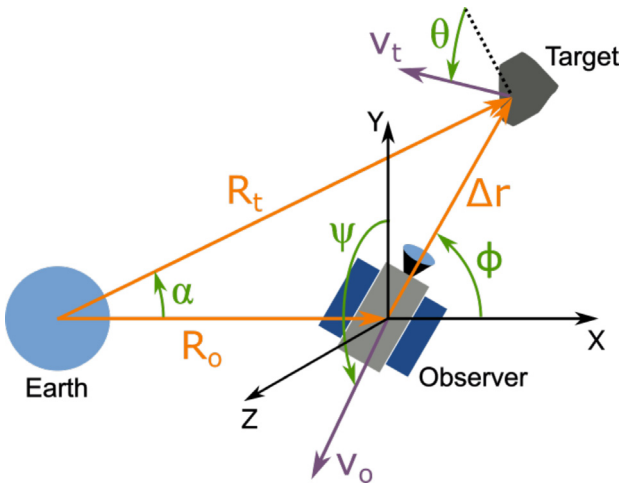


Fig. 3. Diagram of the local reference frame. The displacement vectors have no component along the Z-axis. The observer and target velocity vectors are perpendicular to the Earth–Observer and Earth–Target displacement vectors respectively. Variables are summarised in Table 3.

Table 3
Relative velocity model parameters.

Symbol	Quantity
R_o	Observer distance from the central body
R_t	Target distance from the central body
Δr	Target distance from the observer
ϕ	Target elevation in Local frame
ψ	Observer velocity direction
θ	Target velocity direction

variable is the tangential velocity v_T.

To retrieve an estimate for v_T we consider the observer satellite and the target object to be flying both in a circular orbit. We assume that the net flux of targets is isotropic. We consider the Local right-handed frame satisfying (see Fig. 3):

- O: Centre at the observer satellite.
- X-axis: Parallel to the observer–Earth displacement vector.
- Y-axis: In the direction of the target.

and consider the parameters summarised in Table 3.

The isotropic flux assumption is equivalent to assume that ψ and θ are drawn from a uniform distribution $U(0, 2\pi)$. The position vectors of the observer and the target will then be:

$$\mathbf{r}_o = 0 \tag{12}$$

$$\mathbf{r}_t = \Delta r(\cos\phi \mathbf{e}_x + \sin\phi \mathbf{e}_y) \tag{13}$$

In the approximation of small relative distance $\Delta r \ll R_o$, calling $\epsilon = \frac{\Delta r}{R_o}$, using the cosine law and a first order approximation, we can prove:

$$\begin{aligned} R_t &= \sqrt{R_o^2 + \Delta r^2 + 2R_o\Delta r\cos\phi} \\ &\approx R_o(1 + \epsilon\cos\phi) \end{aligned} \tag{14}$$

and that the angle α that the Earth–Target displacement vector forms with the X-axis is negligible:

$$\begin{aligned} \cos\alpha &= \frac{R_o^2 + R_t^2 - \Delta r^2}{2R_oR_t} \\ &= (1 + \epsilon\cos\phi)(1 - \epsilon\cos\phi) \approx 1 \end{aligned} \tag{15}$$

We can thus write the observer and target velocity vectors:

$$\mathbf{v}_o = v_o(\cos\psi \mathbf{e}_y + \sin\psi \mathbf{e}_z) \tag{16}$$

$$\mathbf{v}_t = v_t(\cos\theta \mathbf{e}_y + \sin\theta \mathbf{e}_z) \tag{17}$$

where, owing to the circular orbit assumption, μ gravitational parameter of the central body:

$$v_o = \sqrt{\frac{\mu}{R_o}} \tag{18}$$

$$\begin{aligned} v_t &= \sqrt{\frac{\mu}{R_t}} \\ &\approx v_o\left(1 - \frac{\epsilon}{2}\cos\phi\right) \end{aligned} \tag{19}$$

The general expression for the relative velocity is:

$$\Delta\mathbf{v} = \mathbf{v}_t - \mathbf{v}_0 - \mathbf{n} \times (\mathbf{r}_t - \mathbf{r}_o) \tag{20}$$

with orbital angular velocity [24]:

$$\mathbf{n} = \frac{R_o\mathbf{e}_x \times \mathbf{v}_o}{R_o^2} \tag{21}$$

By using the first order approximation, we obtain:

$$\frac{\Delta\mathbf{v}}{v_o} \approx \begin{bmatrix} \epsilon\cos\psi\sin\phi \\ \left(1 - \frac{\epsilon}{2}\cos\phi\right)\cos\theta - \cos\psi - \epsilon\cos\psi\cos\phi \\ \left(1 - \frac{\epsilon}{2}\cos\phi\right)\sin\theta - \sin\psi - \epsilon\sin\psi\cos\phi \end{bmatrix} \tag{22}$$

which has norm:

$$\frac{\Delta v}{v_o} = \sqrt{(2 + \epsilon\cos\phi)[1 - \cos(\theta - \psi)]} \tag{23}$$

We define for convenience:

$$\Delta v^* := \frac{\Delta v}{v_o}(2 + \epsilon\cos\phi)^{-\frac{1}{2}} = \sqrt{1 - \cos(\theta - \psi)} \tag{24}$$

and we can retrieve a cumulative distribution function on Δv^* by considering the probability that it is less than a given value z, i.e. $\mathrm{P}(\Delta v^* \leq z)$. This is equivalent to finding the probability $\mathrm{P}(cos(\theta - \psi) \geq 1 - z^2)$. Since θ, ψ are drawn from a uniform distribution $U(0, 2\pi)$, their difference will be drawn from the symmetric triangular distribution centred at zero and with extremes $(-2\pi, 2\pi)$. Because for any angle $\alpha = \alpha + 2k\pi$, the domain of the distribution can be wrapped onto the subdomain $[0, 2\pi)$, yielding again a uniform distribution, $\Delta\theta := (\theta - \psi) \sim U(0, 2\pi)$. In other words, the difference of two uniformly random orientations on the circle will be uniformly random on the circle as well. The problem then simplifies to finding the probability $\mathrm{P}(cos\Delta\theta \geq 1 - z^2)$. This is equivalent to finding the length of the subdomain of $\Delta\theta$ where the condition $cos\Delta\theta \geq 1 - z^2$ is satisfied over the total length 2π of the domain $[0, 2\pi)$. We can verify graphically in Fig. 4 that this yields:

$$F_{\Delta v^*}(z) = \begin{cases} 0 & z < 0 \\ \frac{\arccos(1-z^2)}{\pi} & 0 \leq z \leq \sqrt{2} \\ 1 & z > \sqrt{2} \end{cases} \tag{25}$$

The probability density function (defined for $0 \leq z < \sqrt{2}$) is then:

$$f_{\Delta v^*}(z) = \frac{2}{\pi\sqrt{2 - z^2}} \tag{26}$$

which has expected value:

$$\mathrm{E}[\Delta v^*] = \int_0^{\sqrt{2}} z f_{\Delta v^*}(z) dz = \frac{2\sqrt{2}}{\pi} \tag{27}$$

The tangential component of the velocity can be found as ($\mathbf{v}_P$ velocity component parallel to line of sight of the sensor):

$$\begin{aligned} \mathbf{v}_T &= \Delta\mathbf{v} - \mathbf{v}_P \\ &= \Delta\mathbf{v} - \left(\Delta\mathbf{v} \cdot \frac{\Delta\mathbf{r}}{\Delta r}\right)\frac{\Delta\mathbf{r}}{\Delta r} \end{aligned} \tag{28}$$

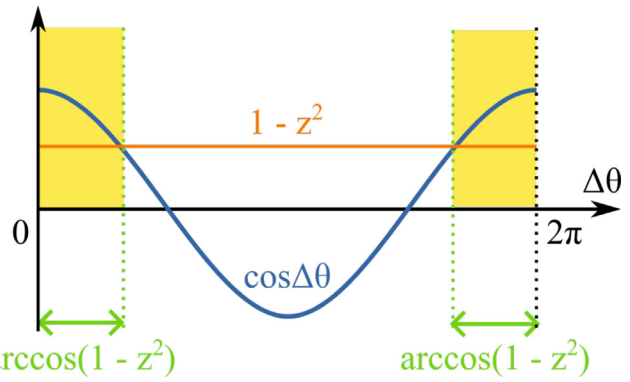


Fig. 4. The yellow-shaded area is the region for which $cos\Delta\theta \geq 1 - z^2$. The total length of the region on the $[0, 2\pi)$ interval is $2\arccos\left(1 - z^2\right)$.

hence:

$$\left(\frac{\mathbf{v}_T}{v_o}\right)_x = (\cos\psi - \cos\theta)\sin\phi\cos\phi + \epsilon\left(\frac{\cos\theta\cos^2\phi\sin\phi}{2} + \cos\psi\sin\phi\right) \tag{29}$$

$$\left(\frac{\mathbf{v}_T}{v_o}\right)_y = (\cos\theta - \cos\psi)\cos^2\phi + \frac{\epsilon}{2}\cos\theta\cos\phi\sin^2\phi - \epsilon\cos\phi\left(\frac{1}{2} + \cos\psi\right) \tag{30}$$

$$\left(\frac{\mathbf{v}_T}{v_o}\right)_z = \sin\theta - \sin\psi - \epsilon\cos\phi\left(\frac{1}{2} + \sin\psi\right) \tag{31}$$

We cannot produce an underlying probability distribution for the tangential velocity analytically as we did before for obtaining Eq. (26). We notice however that it always holds $v_T \leq \Delta v$, and therefore $E[v_T] \leq E[\Delta v]$. Since $E[\Delta v]$ decreases monotonically from $\Phi = 0°$ to $\Phi = 90°$, we can take as an approximation:

$$E[v_T] \approx E[\Delta v\,|_{\Phi=90°}] \approx v_o\frac{2\sqrt{4+2\epsilon}}{\pi} \tag{32}$$

The estimate will underestimate the average tangential velocity and therefore underestimate the maximum observable range as well. Since we are interested in understanding the limits of the constellation design, the small degradation of performance induced by this approximation will not lead to a fundamentally different understanding of the performance drivers of the system. Fig. 5 shows a comparison of our results with a Monte Carlo sampling. We can see how the small relative distance approximation yields an error lower than 7% up to the retrieved maximum observable range of 2000 km.

To find maximum range we use Newton's method through Matlab function `fsolve()`, setting the signal-to-noise threshold $SNR = 5$. This results in the curve in Fig. 6 and in the estimate, for targets of size 10 cm, of a maximum range of approximately 2000 km. This is the target size goal as explained at the beginning of Section 3.

3. Coverage analysis

The goal of our design process is to reliably and continuously observe as many 10 cm targets in the LEO region as possible. We define the LEO region to be the spherical shell comprised between altitudes of 400 km and 1800 km. We choose this specific band of altitudes as it is the one where most of the objects lie. Our objective will then be to maximise the coverage over the shell, and in particular the triple

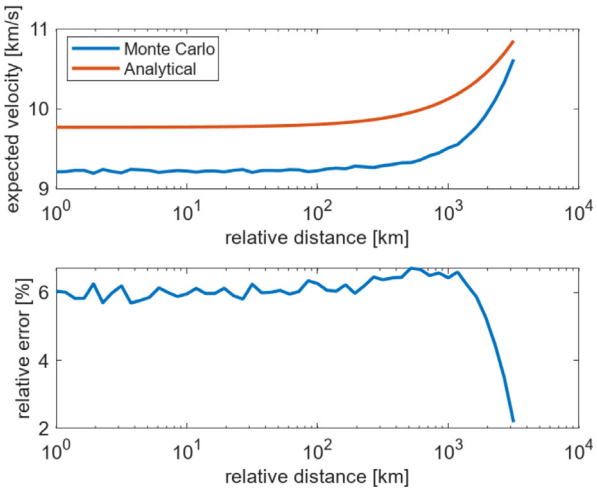


Fig. 5. Analytical estimate for the expected value of the tangential velocity as a function of the relative target–observer distance. Above, a comparison between the analytical estimate and the Monte Carlo simulation. Below, the relative error between the two.

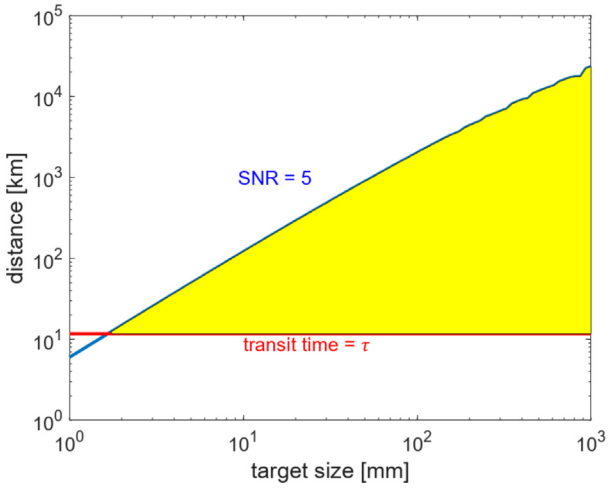


Fig. 6. Maximum observable range against target size. The yellow area is the region for which the target is visible to the observer.

coverage as explained in Section 3.2. We do not consider the specific non-uniform distribution of the current LEO population over the shell as we want our design to be agnostic with respect to the future LEO population.

3.1. Visibility conditions

To understand how much of the sky is covered by the constellation, we first need to understand under which conditions is a target visible to a given observer satellite. In our model, we consider four approximate visibility conditions, expressed as functions of type $f : V_1 \times \cdots \times V_N \to \{0, 1\}$, V_i suitable vector space. For all conditions we have that $\mathbf{r}_t$ is the target's position vector, $\mathbf{r}_o$ is the observer's position vector, $\mathbf{r}_s$ is the Sun position vector, $\Delta\mathbf{r} := \mathbf{r}_t - \mathbf{r}_o$ is the target–observer relative displacement, R is the distance of the Earth's horizon from its centre (in our case, 6471 km, i.e. the average Earth's radius plus the atmospheric height), and D is the maximum observable range. The conditions are (see Fig. 8):

- *Shadowing, or eclipse, condition*: It defines whether the target is outside (true) or inside (false) the Earth's shadow. This condition

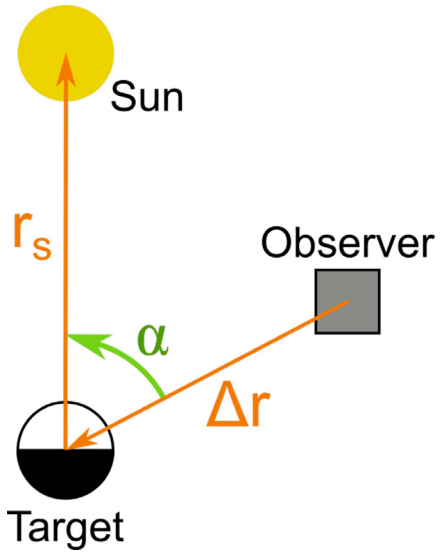


Fig. 7. Phase angle diagram. If $\alpha > 90°$, more than half of the illuminated part of the target body is not reflecting photons back to the observer, and therefore it is not observable as a first approximation.

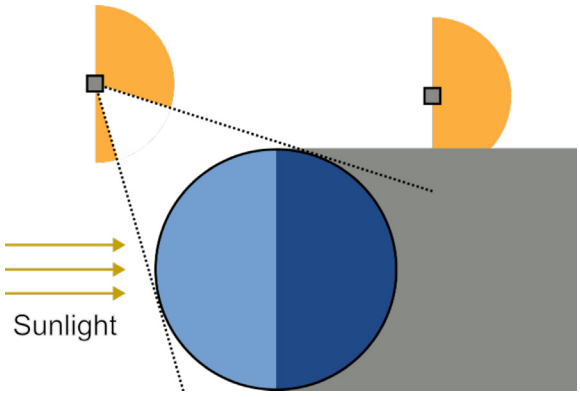


Fig. 8. Possible field-of-regard shapes under the four visibility conditions. The field-of-regard (FOR) is the region where an observation is theoretically possible: when the target is in the orange area, it becomes visible to the observer satellite, represented as a grey square.

is independent of the observer's position. Expressed as:

$$f_{e,1} := \left(\mathbf{r}_t \cdot \mathbf{r}_s > 0\right) \tag{33}$$

$$f_{e,2} := \left[\frac{(\mathbf{r}_t \cdot \mathbf{r}_s)^2}{\|\mathbf{r}_s\|^2} - \|\mathbf{r}_t\|^2 + R^2 < 0\right] \tag{34}$$

$$f_e := f_{e,1} \wedge f_{e,2} \tag{35}$$

- *Above-the-horizon condition*: It defines whether the Earth is occupying (false) or not (true) the target's background view. Expressed as:

$$r_{o,e} := \sqrt{\|\mathbf{r}_o\|^2 - R^2} \tag{36}$$

$$f_o := \left(\|\Delta\mathbf{r}\| r_{o,e} + \Delta\mathbf{r} \cdot \mathbf{r}_o > 0\right) \tag{37}$$

- *Weak scattering condition*: It defines whether the light reflected from the target reaches (true) or not (false) the observer. This is equivalent to asking that the phase angle α in Fig. 7 is less than 90°. For a spherical target, if $\alpha > 90°$, less than 50% of its surface is visible to the observer, enough to assume that it is too faint to be visible. It is assumed that the condition is a good approximation of the statistical behaviour of the target population. It should be noted that r_s is the distance of the Sun from the centre of the Earth, but since the target is much closer to the Earth compared to the Sun we can assume $\mathbf{r}_s - \mathbf{r}_t \approx \mathbf{r}_s$. The condition can be expressed as:

$$f_b := \left(\Delta\mathbf{r} \cdot \mathbf{r}_s < 0\right) \tag{38}$$

- *Maximum range condition*: It defines whether the target is within (true) or above (false) the maximum observable range. Expressed as:

$$f_r := (\|\Delta\mathbf{r}\| - D < 0) \tag{39}$$

Notice that this condition implicitly accounts for factors such as the target reflectivity and the sensor detection capabilities, as they were used in retrieving the maximum observable distance in Section 2.2.

The visibility condition for a given target from a given observer at a specific position of the Sun, true if the target is visible to the observer, is:

$$f_v = f_v(\mathbf{r}_t, \mathbf{r}_o, \mathbf{r}_s) := (f_e \wedge f_o \wedge f_b \wedge f_r) \tag{40}$$

3.2. Coverage definition

For any constellation, given the position of the Sun, the *coverage* at the observation time is the percentage of the volume of the shell that can be accessed by the surveillance system. To understand what we mean by "access" let us consider the case where a target object is shadowed by the Earth, i.e. it is on the opposite side of the region of the Earth illuminated by the Sun. In this case, even if a satellite of the constellation were to pass close to the target and would have it in its field of view, it would not be able to observe it: as no light is received by the target, no photons are reflected from it to the camera. The part of the shell that is shadowed by the Earth is thus the set of points belonging to the shell where the shadowing condition holds, and the volume percentage is the volume of this subset over the total volume of the shell. It is important to notice that, although the shell is fixed, the Sun and the constellation are dynamic in time: what we are interested in is not the coverage at a specific instant, but the average coverage.

As D'Anniballe et al. have shown [20], we need at least three optical measurements of the target to achieve tracking below 200 m accuracy, and therefore our performance metric will be the triple, or three-fold, coverage. This is the percentage of the volume of the shell that can be accessed by at least three satellites of the constellation (see Fig. 9). It may be the case that a target is potentially visible, but lies over the maximum range for all the constellation satellites save for one or two. The point corresponding to the target would therefore be observable, but it would not belong to the triple coverage set. It should be noted that achieving triple coverage is a simplified objective suitable only for preliminary design. In reality, tracking quality over the target population is a function not just of the average number of measurements, but also of the average length of the measurement intervals and the average time between those same intervals. Depending on the number of targets and the tracking accuracy requirements, single or double coverage may be enough. Using the triple coverage criterion is justified here as it guarantees very high tracking accuracy in the best tracking case, while having a high guarantee of excess available sensors that can be used to resolve singular cases at the initial orbit determination stage. The result is a criterion that may thus overestimate the number of required sensors, but that should be suitable for consistent and robust tracking of many targets in the LEO region.

The visibility conditions that a target–observer pair must satisfy to qualify for coverage are those listed in Section 3.1. To define the triple

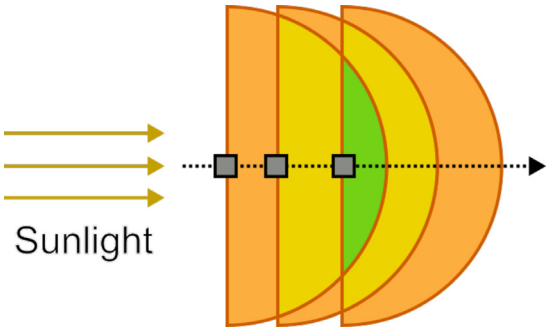


Fig. 9. Example of field-of-regard overlapping for three satellites on the same trajectory. The green area is the triple visibility area.

coverage we consider the set of points within the LEO shell:

$$S = \{\mathbf{r} \in \mathbb{R}^3 \mid 400 \text{ km} < h < 1800 \text{ km}\} \tag{41}$$

and the triple visibility function expressing the truth value of the triple visibility condition:

$$\begin{aligned} f_{v,3} &= f_{v,3}(\mathbf{r}; \mathbf{r}_{o,1}, \dots, \mathbf{r}_{o,N}, \mathbf{r}_s) \\ &:= (\exists \{\mathbf{r}_{o,k}\}_{k=1:3} \subseteq C \mid f_v(\mathbf{r}, \mathbf{r}_{o,k}, \mathbf{r}_s), \\ &\quad \forall k \in \{1,2,3\}) \end{aligned} \tag{42}$$

where C is the set containing the position vectors of the constellation satellites and N is the number of satellites in the constellation. The condition means that we have triple visibility conditions (true) if there are at least three observers within the constellation each satisfying the visibility condition for the given target and Sun direction. The dependency on the constellation and the position of the Sun will be omitted for simplicity, as we assume they are fixed.

Once the sets are defined, the instantaneous triple coverage computation reduces to the computation of an integral:

$$\text{cov}_3 := \frac{1}{V_s} \iiint_S f_{v,3}(\mathbf{r}) dV \tag{43}$$

where $V_s = \frac{4}{3}\pi \left(R_2^3 - R_1^3\right)$ is the volume of the shell (in our case, $h_2 = 1800$ km, $h_1 = 400$ km, $R_j = R_E + h_j$, R_E Earth's radius). Whenever the constellation is not fixed in time, the instantaneous triple coverage will be in general time-dependent as the relative positions of the observers and the targets will vary even over time intervals where the Earth–Sun motion is negligible. Among the visibility conditions above we neglected the one referring to the relative position vector being within the field of view of the sensor, here assumed to be 5 degrees. The reason why this does not concern our analysis is that we are assuming the observer satellite will steer whenever prompted to observe a specific target, changing its attitude to point in the right direction. Since there are no constraints on the attitude, this allows the observer to do a 360-degree covering of the surrounding sky. In a more detailed analysis, this may however become a pressing issue: whenever the observer satellite is pointing in one specific direction, it is losing all the measurement opportunities in the other directions.

To properly cover for this issue, a proper sky surveying and target tracking strategy is needed. A possibility could involve predicting what is the direction the desired target at every fixed timestep, pointing in that direction, and collecting the resulting angular measurements. As long as the predictions are accurate enough, the desired target should lie within the FOV of at least one sensor most of the time. Multiple target tracking would require more sophisticated and collaborative solutions, segmenting each field-of-regard in regions with sizes comparable to the FOV and optimising the pointing directions as to maximise the increase in the average position accuracy. Similar tracking solutions have been used for ground systems, as surveyed in Xue et al. (2024) [25]. Another consideration regards the possibility of tracking multiple targets within a single FOV, which we assume to be possible following strategies similar to Jiang et al. (2022) [26].

Table 4
Walker-Delta constellation parameters.

Symbol	Quantity	Search space	Unit
N_o	Number of orbits	≥1	–
$N_{sat/o}$	Number of satellites per orbit	$[N_o, 65]$	–
h	Altitude	460	km
i	Inclination	[75, 80]	°
Ω_0	Right ascension (first orbit)	0	°
$\Delta\theta$	Orbital phase	$\left[0, \frac{360}{N_{sat/o}}\right)$	°

3.3. Constellation geometry

The main architecture that we will analyse in this work is the Walker-Delta constellation [27]. The choice is guided by two main reasons: the highly symmetric nature of the architecture goes well with the aim of covering any potential population distribution, while the low number of parameters makes parametric analyses and optimisation feasible with a low amount of computational resources. We assume that the constellation geometry is fixed in the ECI frame (i.e. perturbation effects are negligible) thanks to periodic manoeuvring capabilities for orbit raising. As we will see in Section 3.5, the average yearly coverage of the constellation is approximately independent of its RAAN, thus justifying us in neglecting the Earth oblateness effects. The parameters of a Walker-Delta constellation, together with their search spaces, are summarised in Table 4. The search spaces will be relevant in the optimisation procedure described in Section 4.2, which aims to find the constellation parameters that maximise the average triple coverage of the system as defined in Section 3.2.

The constraints on the search space are retrieved as follows:

- The number of satellites per orbit $N_{sat/o}$ is not greater than 65 to avoid the coverage saturation effects. The upper bound 65 is chosen as not to have more than three observer satellites within the maximum observable range, limiting the percentage of volume in which more than three measurements would be available. The lower limit equal to the number of orbits is set to guarantee a low number of orbits for a given satellite budget. This is justified by the fact that it is easier to place a sequence of satellites in the same orbit after launch.
- The altitude h should be as high as possible to maximise the constellation lifetime and therefore the total number of observations over the mission time. However, assuming the constellation is a network of small satellites with limited reliability, a satellite placed at too high an altitude may become a long-term danger for satellites placed in lower orbit as debris if it fails. To solve this conundrum, we set the constellation altitude to be compliant with recent ESA guidelines for satellites with no recurring manoeuvring capabilities, setting the maximum orbital lifetime to 5 years [28]. Assuming as in Pineau et al. [21] the satellites are 16U Cubesats with a mass of 40 kg and the ECSS-E-ST-10-04C standard for the solar flux [29], Fig. 10 shows the satellite expected lifetime from the beginning of 2025 as computed by the ESA Drama software [30] at a starting altitude of 460 km. We can observe that the altitude is compliant with the lifetime requirements, and therefore it is chosen as a design point for the constellation.
- The lower limit on the inclination i is given by the constraint that the poles at an altitude of 400 km should be observable with the given maximum range, as per Fig. 11. It holds approximately $\cos i_{min} \approx \frac{D}{R_e+h}$, D maximum range, R_e mean Earth radius, h constellation altitude. This approximately corresponds to 66 degrees. Polar inclinations are avoided to limit overlapping between orbits, while retrograde orbits are removed as the average coverage is not dependent on the direction of motion of the constellation satellites. The inclination bounds are further

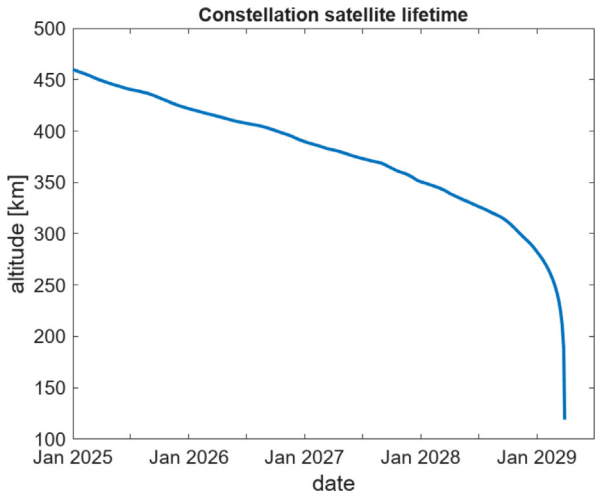


Fig. 10. Natural lifetime of a constellation satellite failure after failure, and thus without manoeuvring capabilities, placed at an altitude of 460 km. Simulation performed with the ESA Drama software [30] using the ECSS-E-ST-10-04C standard for the solar flux [29].

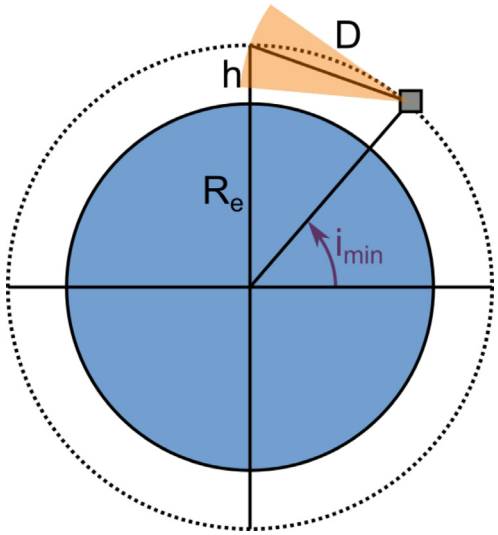


Fig. 11. Diagram of minimum inclination for an observer satellite to be able to see the polar region. D is the maximum range and h is the constellation altitude.

reduced to be between 75° and 80° to contain the yearly coverage variation as explained in Section 3.5.

- Ω_0 only affects the dynamics of the triple coverage and not its yearly average, as explained in Section 3.5. Since we are only interested in the average performance, we set the parameter to 0 rad.
- The constellation repeats itself after a phase shift $\Delta\theta$ of $\frac{360}{N_{sat/o}}$ degrees.

3.4. Monte Carlo integration

The design process will focus on finding the optimal parameters of the Walker-Delta architecture maximising the triple coverage of the surveillance system given a budget in terms of the total number of satellites of the constellation. To search for the optimal solution, we need a method for estimating the coverage of the satellite network. As we have seen in Section 3.2, the problem of computing the coverage reduces to the problem of computing a volume integral over the LEO shell. A general enough method should be able to cope with strongly nonlinear visibility functions and with any domain shape, as in applications outside the scope of this paper we may not want to compute the coverage just over a spherical shell but on an arbitrary volume. Moreover, any good integration method should also provide some bounds on the integration error behaviour. A potential robust solution is to use Monte Carlo integration [31]. The idea is to sample a population over the integration volume and use it to compute an unbiased estimator for the integral. In our case, given a sample population $\{\mathbf{r}_1, \dots, \mathbf{r}_{n_{MC}}\}$, the triple coverage estimator is:

$$cov_{3,MC} = \frac{1}{n_{MC}} \sum_{k=1}^{n_{MC}} f_{v,3}(\mathbf{r}_k) \tag{44}$$

To make this estimator unbiased, i.e. such that $\mathrm{E}\left[cov_3\right] = \mathrm{E}\left[cov_{3,MC}\right]$, the population should be sampled uniformly over the spherical LEO shell. We consider the position vectors in spherical coordinates (r, θ, ψ) corresponding to radius, inclination and azimuth such that for a given point:

$$\begin{cases} x_k = r_k \sin\theta_k \cos\psi_k \\ y_k = r_k \sin\theta_k \sin\psi_k \\ z_k = r_k \cos\theta_k \end{cases} \tag{45}$$

In this case, choosing a uniform sampling over the spherical coordinates would not yield an unbiased estimator as points would have a higher probability of being sampled near the poles of the sphere and at lower altitudes. This issue can be solved analytically without resorting to rejection sampling. We consider three uniform random variables each sampled from a uniform distribution $\left(\xi_r, \xi_\theta, \xi_\psi\right) \sim U(0,1)$. Since the random variables are uniform, we can write the three-dimensional infinitesimal volume element of the shell as:

$$dV = V_s d\xi_r d\xi_\theta d\xi_\psi \tag{46}$$

where V_s is the volume of the shell. By writing the volume element in spherical coordinates we obtain:

$$V_s d\xi_r d\xi_\theta d\xi_\psi = r^2 \sin\theta dr d\theta d\psi \tag{47}$$

This equation can be decoupled into the following three ordinary differential equations, assuming $V_s = K_r K_\theta K_\psi$:

$$\begin{cases} K_r \frac{d\xi_r}{dr} &= r^2 \\ K_\theta \frac{d\xi_\theta}{d\theta} &= \sin\theta \\ K_\psi \frac{d\xi_\psi}{d\psi} &= 1 \end{cases} \tag{48}$$

subject to the boundary conditions (R_1 and R_2 lower and upper radius of the spherical shell respectively):

$$\begin{cases} \xi_r(R_1) = 0, \quad \xi_r(R_2) = 1 \\ \xi_\theta(0) = 0, \quad \xi_\theta(\pi) = 1 \\ \xi_\psi(0) = 0, \quad \xi_\psi(2\pi) = 1 \end{cases} \tag{49}$$

This problem can be solved analytically, allowing us to obtain the following relationships for uniform sampling on the spherical shell:

$$\begin{cases} r &= \sqrt[3]{R_1^3 + \xi_r\left(R_2^3 - R_1^3\right)} \\ \theta &= \arccos\left(1 - 2\xi_\theta\right) \\ \psi &= 2\pi\xi_\psi \end{cases} \tag{50}$$

The resulting simple method is summarised in Algorithm 1, where *initialise_uniform_sampling* is the function initialising the uniformly sampled target population on the spherical shell and *get_visibility* is the function computing the visibility function for the given target.

Algorithm 1 Monte Carlo coverage computation

Input: $\{\mathbf{r}_{o,k}\}_{k=1:N}$, $\mathbf{r}_s$, n_{MC}
Output: *coverage*

```
{r_{t,j}}_{j=1:n_MC} ← initialise_uniform_sampling(n_MC)
coverage ← 0
j ← 1
while j < n_MC do
    visibility = get_visibility(r_{t,j}, {r_{o,k}}_{k=1:N}, r_s)
    coverage ← coverage + visibility
    j++
end while
coverage ← coverage / n_MC
```

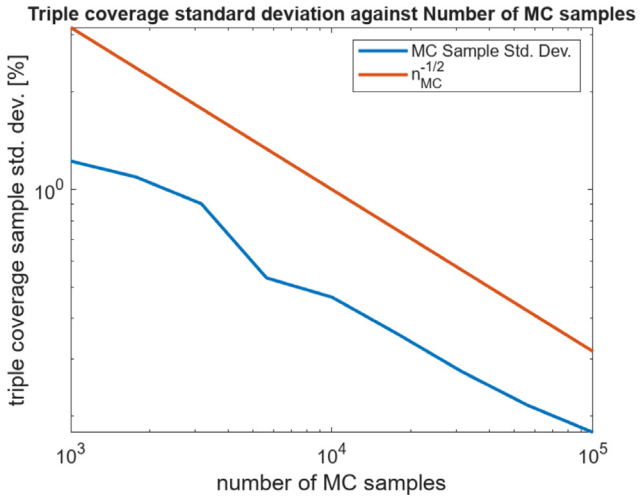


Fig. 12. Triple coverage sample standard deviation against number of Monte Carlo samples.

To retrieve the error behaviour, we test the algorithm on the case of triple coverage estimation for a constellation with parameters (N_o, $N_{sat/o}$, h, i, Ω_0, $\Delta\theta$) = (8, 50, 460 km, 70°, 0°, 5°), with the parameters defined in Table 4. We run the algorithm for n_{MC} between 10^3 and 10^5. Values outside this range are omitted as either too inaccurate or too computationally intensive. For each n_{MC}, we initialise 20 sample populations. For each sample population, we compute the corresponding coverage estimate. Using the coverage estimates, we compute for each n_{MC} mean and sample variance. Fig. 12 shows how the sample standard deviation $S := \sqrt{Var}$ approximately decreases as $k/\sqrt{n_{MC}}$, in accordance with the theory, k arbitrary constant. Since the sample variance is an unbiased estimate of the true variance, this is an estimate for the integration error. In particular, we can observe that to reduce the error by one order of magnitude, we need to increase n_{MC} by two orders of magnitude. Moreover, for $n_{MC} = 10^4$ the absolute error on the triple coverage is less than 1%. This means that we can retrieve a decent estimate for the coverage without using too much computational resources. For these reasons, in all the simulations we will use $n_{MC} = 10^4$ (unless otherwise stated).

Compared to the algorithms developed by Biria et al. [17] and Sun et al. [19], this method has the disadvantage of being more computationally expensive. However, the strong point of the algorithm lies in its simplicity and versatility: no assumptions where made on the nature of the coverage function, and with little modification the algorithm can handle non-uniform target populations with non-uniform sampling.

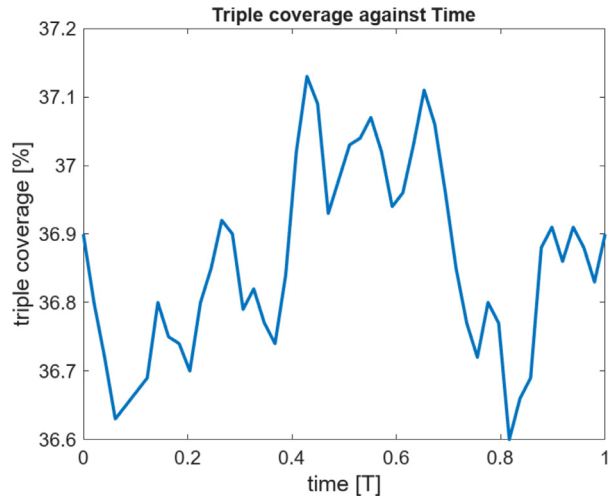


Fig. 13. Time variation of triple coverage. The time is measured as a fraction of the period T of the constellation.

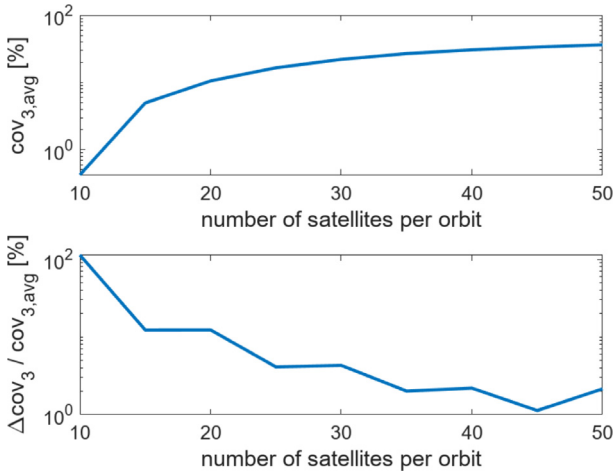


Fig. 14. Time variation of triple coverage against number of satellites per constellation orbit. Above, the mean triple coverage per $N_{sat/o}$. Below, the ratio between $\Delta cov_3 = max_t(cov_3(t)) - min_t(cov_3(t))$ and the average triple coverage per $N_{sat/o}$.

3.5. Time-dependent effects

The methods we discussed above are used for the computation of the instantaneous coverage. In general, this is different from the average coverage over a long time period. The reason is that, although the LEO shell is static in the ECI frame, the constellation satellites and the Sun–Earth system are in motion. This creates two periodic effects on the coverage: a short-term one, with a period of a few minutes to about one hour, related to the motion of the constellation, and a long-term one, with a period of a few months, related to the revolution of the Earth around the Sun. The two very different dynamics allow us to decouple the two effects and analyse them separately. Fig. 13 shows the short-term instantaneous triple coverage variation for a test constellation with parameters (N_o, $N_{sat/o}$, h, i, Ω_0, $\Delta\theta$) = (8, 50, 460 km, 70°, 0°, 5°), while Fig. 14 shows the difference between maximum and minimum coverage over the orbital period for varying $N_{sat/o}$ with the other parameters as the test constellation. We can observe that, for constellations with more than 30 satellites per orbit, the coverage variation is less than the Monte Carlo integration error for $n_{MC} = 10^4$ and therefore it is negligible.

Fig. 15 shows the yearly variability of the triple coverage of the reference constellation. We can observe two effects: the three main

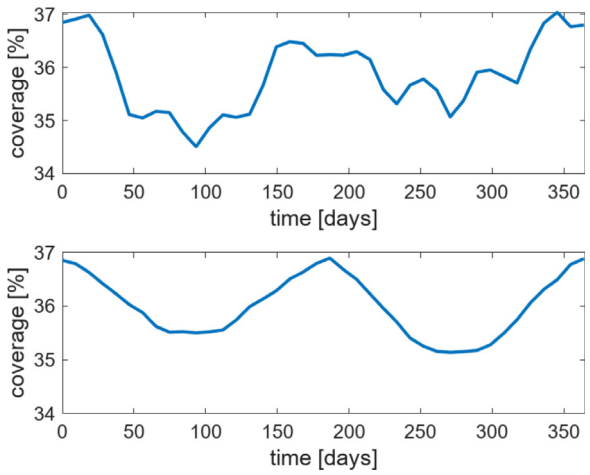


Fig. 15. Yearly triple coverage, varying owing to the variation of the Sun–Earth displacement. Above, the combined effect of the azimuthal and elevation variation of the Sun's direction. Below, elevation effects only.

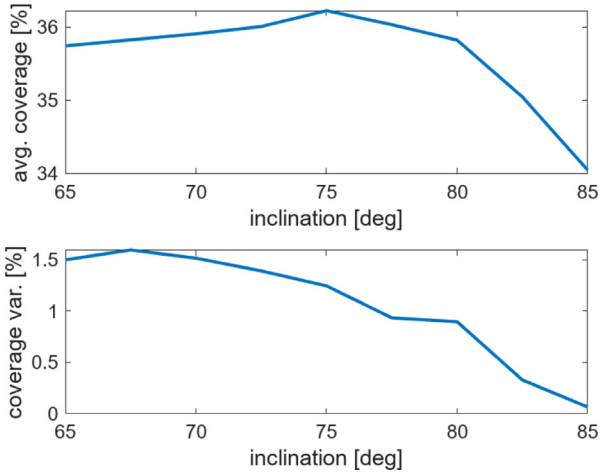


Fig. 16. Yearly triple coverage against constellation inclination, considering only the change in the elevation of the Sun direction. Above, the average yearly triple coverage. Below, the yearly triple coverage variation computed as the difference between the maximum and the minimum coverage.

peaks are due to the change in the elevation of the Sun, which varies from Summer to Winter between +23.4°and −23.4°. A second effect with a higher frequency is due to the azimuthal variation of the Sun's direction, which changes how many orbits fall within the Earth's shadow. This second effect is smaller, equal for all constellations with the same N_o, averaging out over the year and therefore neglected in subsequent analyses. Fig. 16 shows the average yearly triple coverage and the difference between the maximum and minimum yearly triple coverage for varying constellation inclination, owing only to the change in the elevation of the Sun. We can observe that this effect causes a coverage variation between 0.4 and 1.6%, in the order of the Monte Carlo estimation error for inclinations higher than 75°.

We can restrict the inclination search space to the interval [75°, 80°] by observing this range has both high average coverage and low coverage variation (within 1%). Thanks to the low coverage variation, we can estimate the triple coverage by computing it for any one arbitrary Sun direction (in our simulations, we consider the Sun at the Autumn equinox unless otherwise stated). This allows us to greatly reduce the computational burden as the coverage will be estimated with just one Monte Carlo integration run at one instant, without losing information important for the design in the process as long as we accept a coverage error of about 1%. Unless otherwise stated, all the simulations in the following section will follow this coverage computation methodology. Moreover, since all the constellations differing only for their Ω_0 will have different coverage only due to the different azimuthal position of the Sun, and because this effect averages out over one year, we will take as a design point $\Omega_0 = 0$.

4. Constellation design

In this section, all the tools developed above will be applied to the actual design of the constellation. First, the theoretical coverage limits for a given number of constellation satellites budget and its dependency on the constellation inclination will be explored through tradespace analysis. Then, a random search method will be used to find an optimal constellation in terms of triple coverage. The robustness of the design will be tested with a random satellite loss analysis. Different deployment methods will be compared to understand how to better optimise launch sequences to achieve good coverage as soon as possible. Finally, an architecture for reaching good coverage with a strong satellite budget constraint will be discussed.

4.1. Tradespace analysis

The available budget will, in general, impact many aspects of the surveillance mission: how good of a sensor one gets, how stable or heavy a satellite is, and how many launches can be afforded. To simplify, we will assume that the mission cost will grow linearly with the number N of satellites making up the constellation, which will be the mission budget. To understand how the attainable coverage depends on the budget, we set a fixed number of satellites N and we randomise all the other parameters while satisfying the constraint $N = N_o N_{sat/o}$, with N_o and $N_{sat/o}$ as defined in Table 4. Notice that N_o is randomised as well and independent from N, with $N_{sat/o}$ that can be retrieved from both N and N_o.

Fig. 17 shows the tradespace plot for the triple coverage with the Pareto front of the parameter space for N between 100 and 1000. We can notice that there are many solutions near the Pareto front, while those away from it lie on the same line, suggesting they correspond to cases where the constellation has one or two orbits and a high number of satellites per orbit, yielding coverage saturation.

In Section 3.5, we developed a discussion on the yearly coverage variability as a function of the constellation inclination, restricting the inclination search space to the interval [75°, 80°]. To have a better idea of the dependence of coverage on the constellation inclination, we run a parametric analysis considering fixed constellation parameters ($N_{sat/o}$, h, Ω_0, $\Delta\theta$) = (50, 460 km, 0°, 5°) and N_o varying between 6 and 8. The results are shown in Fig. 18, where it is evident that the optimal performance lies for inclinations between 65° and 85°, compatible with the minimum inclination estimate of Section 3.3 and confirming the analysis of Section 3.5.

4.2. Optimisation procedure

We define the design problem as a triple coverage maximisation problem. We assume here the independent variables of the triple coverage function to be the constellation parameters summarised in Table 4, such that:

$$cov_3 = cov_3(\mathbf{p}) \tag{51}$$

where $\mathbf{p} := \left(N_o, N_{sat/o}, i, \Delta\theta\right)$ is the parameter vector, with h and Ω_0 removed as they are fixed at 460 km and 0° respectively. The maximisation problem is then to find:

$$\mathbf{p}_{opt} = \arg\max_{\mathbf{p}\in\mathcal{P}} cov_3(\mathbf{p}) \tag{52}$$

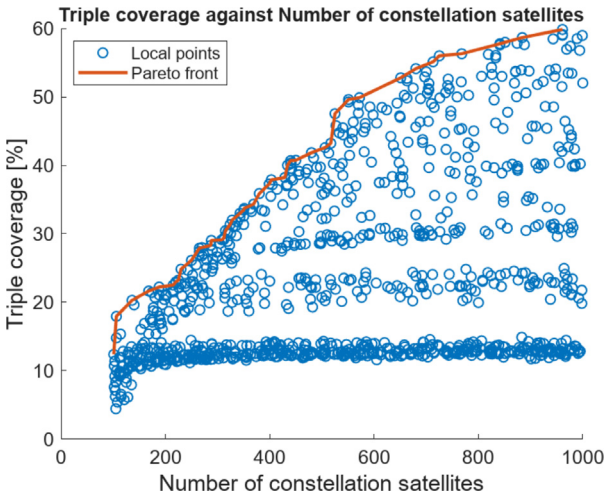


Fig. 17. Tradespace exploration. Each point corresponds to a specific set of parameters sampled randomly from the search space. The band structure is due to the integer nature of the N_o and $N_{sat/o}$ parameters. For instance, the first band from below corresponds to $N_o = 1$. In orange, the Pareto front for the constellation architecture. Notice that the front is just an estimate based on random assignment, and therefore it is an underestimation of the actual front.

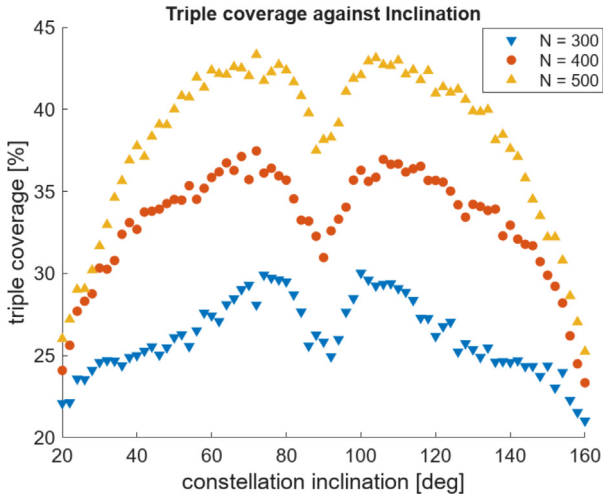


Fig. 18. Triple coverage as a function of the constellation inclination. The fixed constellation parameters are $(N_{sat/o}, h, \Omega_0, \Delta\theta) = (50, 460\text{ km}, 0°, 5°)$.

where:

$$\begin{aligned}\mathcal{P} := \{&\left(N_o, N_{sat/o}, i, \Delta\theta\right) \mid \\ &N - \Delta N \leq N_o N_{sat/o} \leq N + \Delta N, \\ &N_o \leq N_{sat,o}, \\ &i \in \left[75°, 80°\right], \Delta\theta \in \left[0°, \frac{360°}{N_{sat/o}}\right)\}\end{aligned} \tag{53}$$

is the constrained search space for the parameters. It should be noted that the constraint $N = N_o N_{sat/o}$ was substituted by a more relaxed one where the budget is within an interval $[N - \Delta N, N + \Delta N]$. This choice is motivated by the fact that the constraint would otherwise be too strong: if N were a prime number, the set of solutions would be characterised by $N_o = 1$, which would be sub-optimal in all cases as the one available orbit would quickly saturate and many satellites would be wasted. The solution to this problem is in general not unique and cannot be found analytically or with gradient descent methods as the coverage function is not differentiable everywhere. Moreover, as a mixed integer nonlinear optimisation problem with nonlinear integer constraints, the search problem will likely have many suboptimal local minima.

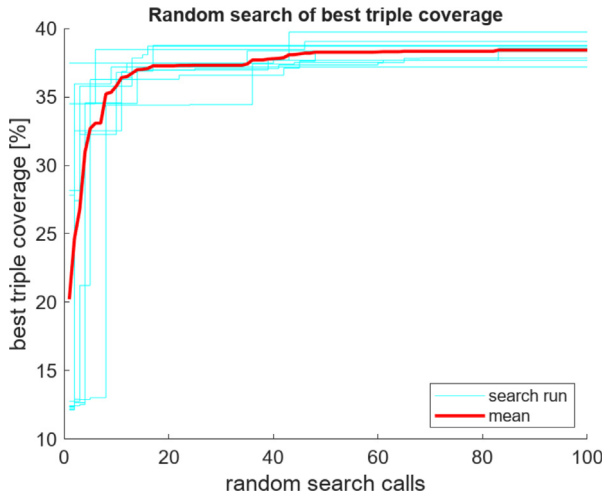


Fig. 19. Constellation optimisation using random search, $N = 400$, $\Delta N = 5$. In cyan, the single random search runs. In red, their averages. A solution lying near the Pareto front is found on average after only 20 function calls.

Table 5
Optimal constellation parameters, $N = 400$, $\Delta N = 5$, obtained using random search as explained in Section 4.2 using the search space in Table 4.

Symbol	Quantity	Optimal	Unit
N_o	Number of orbits	15	–
$N_{sat/o}$	Number of satellites per orbit	27	–
h	Altitude	460	km
i	Inclination	77.1	°
Ω_0	Right ascension (first orbit)	0	°
$\Delta\theta$	Orbital phase	8.5	°
cov_3	Triple coverage	38.7	%

The parameter with the most impact within the search space in Table 4 is the number of orbits, especially when it is very low. Looking at Fig. 17, the emerging band structure is given by the discrete nature of the N_o parameter, while the other parameters determine a lower variation in the performance. Given the low size of the integer parameters space, a method with good enough exploration capabilities in this case is a simple random search over the interval $[N - \Delta N, N + \Delta N]$ and selecting the best solution among all the found ones, knowing that the worse performance on the exploitation of the real-valued parameters is far outclassed by the superior exploration capacity on the integer-valued ones. Fig. 19 shows a random search run for the $N = 400$, $\Delta N = 5$, plotting the best coverage against the number of function calls. $N = 400$ is an arbitrary test case which was chosen to both have an expected coverage of around a third of the spherical shell, as per Fig. 17, and to keep all simulations within one hour of required computer time.[1]

Table 5 shows the best parameters found by the search algorithm. In Walker notation [32], these approximately correspond to a 77°: 405/15/10 constellation, where 10 is the phase factor. Fig. 20 shows a plot of the constellation, while Fig. 21 plots a two-dimensional projection of the covered surface at an altitude of 550 km, where the object population peaks in LEO.

4.3. Robustness analysis

A large surveillance constellation should be able to yield good performance even after multiple satellite failures, an event not unlikely

[1] All simulations were implemented as Matlab scripts and run on a laptop with a Ryzen 5 5600H processor and 16 GB RAM.

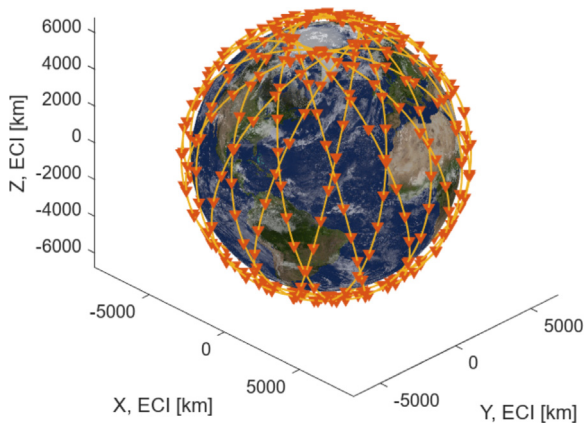


Fig. 20. Optimal constellation. Notice that the constellation is not fixed with respect to the Earth's surface due to the Earth's rotation.

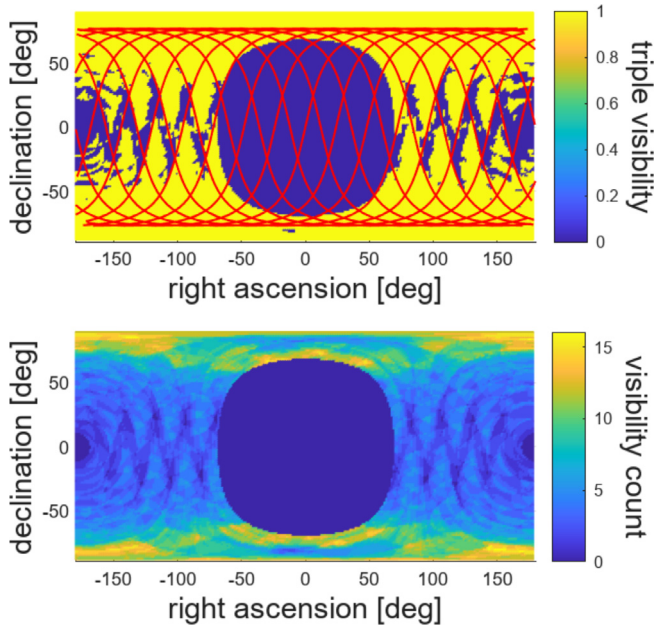


Fig. 21. Visibility map of the optimal constellation in the ECI frame at 550 km altitude during the Autumn equinox. Above, the yellow-shaded area is the area under triple visibility conditions and the red trajectories are the tracks of the constellation. Below, the visibility count for the optimal constellation at 550 km altitude. A visibility count of three or more means that the target is under triple visibility conditions. The large hole at the centre corresponds to the surface area under eclipse conditions.

in the case of the usage of nanosatellites. To check for the robustness of the design we let the satellites fail randomly one by one up to 10% of the constellation, each time computing again the triple coverage of the surviving system. Since satellites can fail anywhere, the surviving part of the constellation may lose its symmetry, invalidating part of the discussion of Section 3.5. However, we can still compute the coverage at only one timestep if we neglect the eclipse and the blinding condition, as the coverage function becomes time-independent in this case. This makes our coverage estimates wrong, but it is not important in this case as our goal is not to compute accurately the triple coverage of the system, but just to estimate the loss in coverage after multiple satellite losses. The effects of the Sun can be neglected as on average they will not the impact of the satellite loss on the coverage. Fig. 22 shows 20 satellite loss runs together with their average, with the triple coverage efficiency on the y-axis, i.e. the ratio between the triple coverage of the surviving system and the triple coverage of the healthy system,

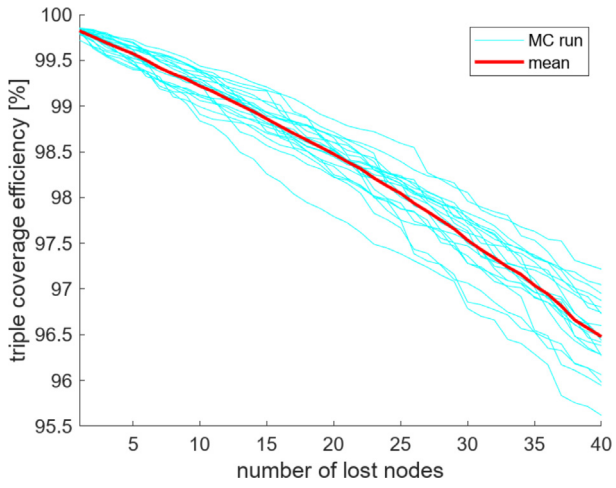


Fig. 22. Satellite loss analysis for random satellite loss in the optimal constellation of Table 5. In cyan, single Monte Carlo runs. In red, the average satellite loss behaviour. The triple coverage efficiency is defined as $\epsilon_{cov,3} := \frac{cov_{3,surv}}{cov_{3,healthy}}$.

$\epsilon_{cov,3} := \frac{cov_{3,surv}}{cov_{3,healthy}}$. We can observe that even in the worst case the coverage loss is less than 5%, and on average about 3%, much less than the 10% total satellite loss, making the system very robust.

4.4. Deployment strategy

Large-scale distributed systems may require a significant amount of time in their deployment. In the case of large constellations, these time windows may extend up to a few years. To maximise the return on the investment, we want to get significant performance as quickly as possible, even with partial deployment. We analyse here the behaviour of three different deployment strategies. We assume we are launching 9-satellite batches, each targeting a single orbit with true anomaly spacing $(\theta_k - \theta_{k-1}) = \frac{2\pi}{N_{sat/o}}$:

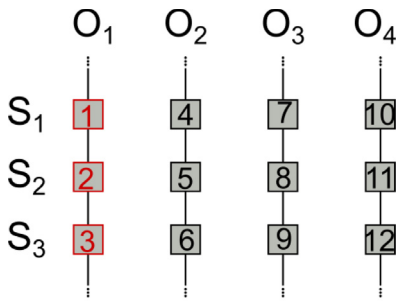
- *Full orbit first*: each constellation orbit is completely populated before targeting the next orbit.
- *Consecutive orbits*: batches populate consecutive orbits as shown in Fig. 23.
- *Random*: batches are deployed both in a random slot and in a random orbit.

The two non-random strategies are schematically summarised in Fig. 23.

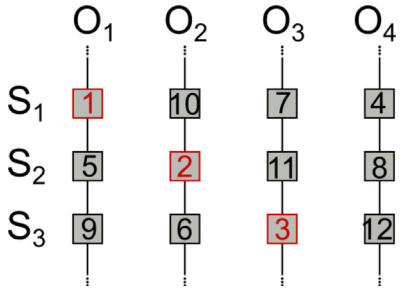
Fig. 24 shows the behaviour of the three strategies in terms of coverage efficiency $\epsilon_{cov,3} := \frac{cov_{3,deployed}}{cov_{3,full}}$. We can observe that *fullOrbitFirst* has the fastest dynamic at first, meaning that it has the highest coverage increase within the first few launches. After twelve launches, *consecutiveOrbits* becomes the better strategy, as *fullOrbitFirst* suffers from triple coverage saturation near the poles. The *random* strategy sits somewhere in between as a less extreme case.

4.5. Low-budget architecture

Even with an optimistic forecast of the technological development of the near future, it is difficult to envision a constellation of hundreds of satellites carrying high-quality optical instrumentation costing less than hundreds of millions of dollars. Some of the results of the previous sections, however, point in the direction of lower-budget architectures. First, the realised triple coverage is split between nearby satellites on the same orbit and satellites on different orbits passing at the same time at high inclinations, while having a visibility count waste near the



(a) Full orbit first



(b) Consecutive orbits

Fig. 23. Schematic diagrams of the non-random deployment strategies. O_k indicates the orbit k, S_j indicates the orbital slot j. The first three deployed batches are in red to better highlight the deployment order.

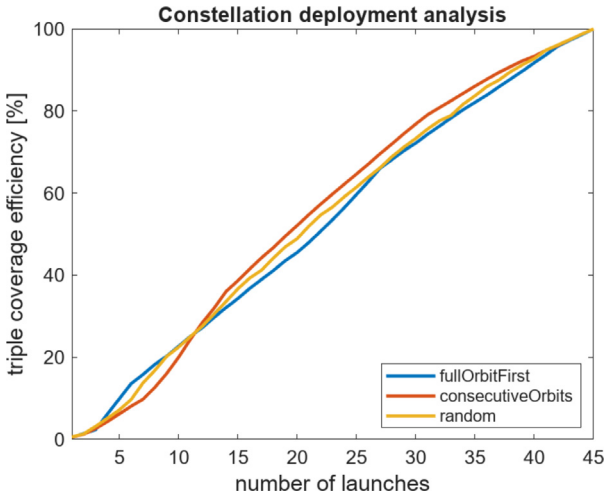
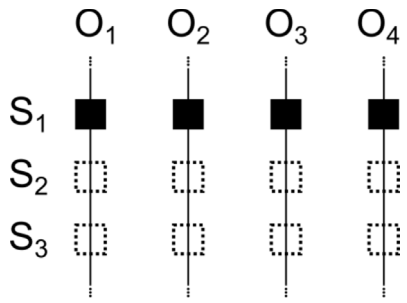


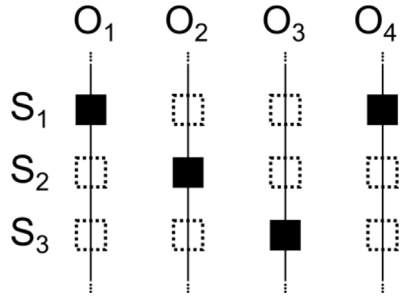
Fig. 24. Comparison of the different deployment strategies for the optimal constellation of Table 5. The triple coverage efficiency is defined as $\epsilon_{cov,3} := \frac{cov_{3,deployed}}{cov_{3,full}}$.

poles as shown in Fig. 21. Moreover, careful deployment of batches of satellites can achieve lower but still significant levels of instantaneous coverage.

A possible approach to evaluate the performance of a low-budget architecture is to analyse it with respect to relaxed versions of the original requirements. In the previous section, we considered as a performance metric the *instantaneous triple coverage*, i.e. the percentage of the sky that was visible to at least three observers at any given time, and its time average (in the case of a Walker-Delta constellation, the two are similar as we have shown in Section 3.5). This time we consider the *cumulative triple coverage* instead: a portion of the sky is considered in this condition if it is in triple coverage condition at least one time over the constellation period. A high average instantaneous



(a) Overlapped



(b) Not overlapped

Fig. 25. Schematic diagrams of the two low-budget configurations.

triple coverage would require that the sky is visible at almost all times over the constellation orbital period, but the cumulative triple visibility condition only requires that this happens at one time instant. Indeed, we may only be interested in covering the sky periodically if we only required surveillance information over time windows longer than the constellation orbit. Formally, we can express the condition as:

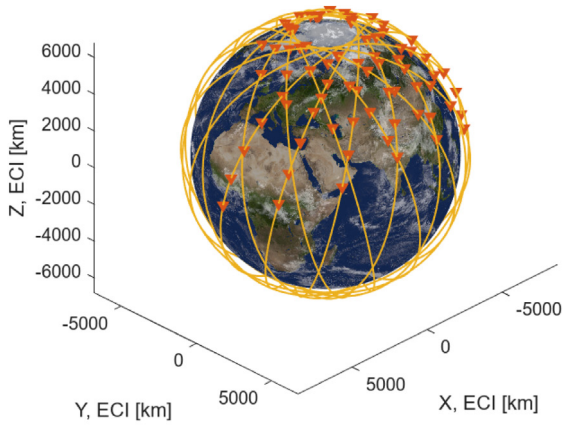
$$f_{cv,3} : \exists t \in [0, T) \mid f_{v,3}(\mathbf{r}, \mathbf{r}_{o,1}, \dots, \mathbf{r}_{o,N}, \mathbf{r}_s) \tag{54}$$

where $f_{v,3}$ is the triple visibility condition as expressed in Section 3.2. The cumulative triple coverage condition can then be computed using the condition above in the same way as we did for the instantaneous triple coverage, using Eq. (43). Operationally, the cumulative coverage is computed by propagating the constellation according to Keplerian dynamics and computing the instantaneous coverage at each time step using the Monte Carlo integration method as explained in Section 3.4.

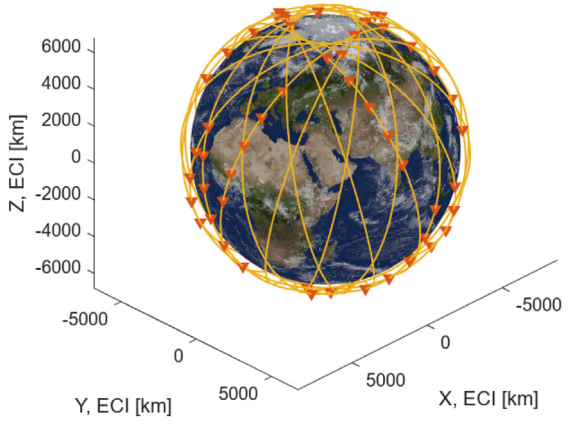
Informed by the results of the deployment analysis, we now consider a constellation of N_o batches of five satellites lying close together with a true anomaly separation $(\theta_k - \theta_{k-1}) = \frac{2\pi}{N_{sat/o,W}}$ on the orbits of a Walker-Delta constellation, where θ is the true anomaly and k is the orbit index. Notice that N_o and $N_{sat/o,W}$ refer to the optimal parameters of the equivalent Walker-Delta constellation of N satellites that shares the same geometry as the low-budget constellation, while $N_{sat/o,L}$ is the number of satellites per orbit (and therefore per batch) for the low-budget constellation. We analyse two cases for the true anomaly phase between batches of successive orbits, as shown in Fig. 25:

- *Overlapped*: Most satellite batches have field-of-regard overlapping near the poles.
- *Not overlapped*: Field-of-regard overlapping between different satellite batches near the poles is avoided.

Fig. 26 shows a plot of the two constellation types in ECI frame for $N_{sat/o,L} = 5$, while Fig. 27 shows a plot of the instantaneous triple coverage and cumulative triple coverage against time for the two cases. We can observe that the overlapped constellation performs significantly better, thanks to the fact that it is able to realise triple coverage with



(a) Overlapped



(b) Not overlapped

Fig. 26. Low-budget constellation configurations (ECI frame, $N_{sat/o,L} = 5$).

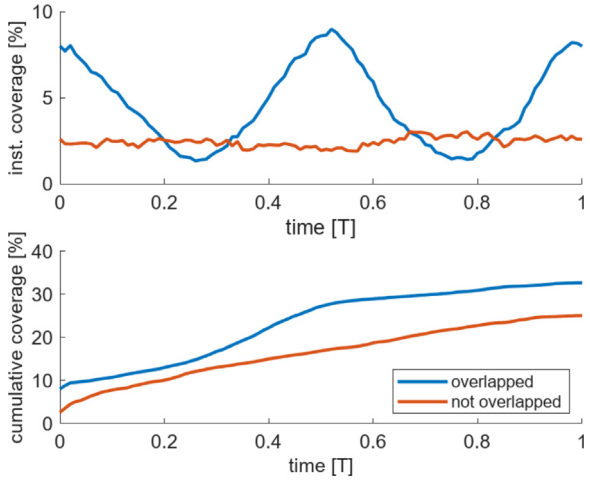


Fig. 27. Comparison of overlapped and non-overlapped low-budget configurations performance, $N_{sat/o,L} = 5$. The time is measured as a fraction of the period T of the constellation.

satellite batches of different orbits near the poles, corresponding to the instantaneous triple coverage peaks every half-period.

Fig. 28 shows a comparison for the overlapped constellation case with varying $N_{sat/o,L}$. We can see how for $N_{sat/o,L} > 7$ there is a diminishing return on performance. Moreover, using only 3 satellites per

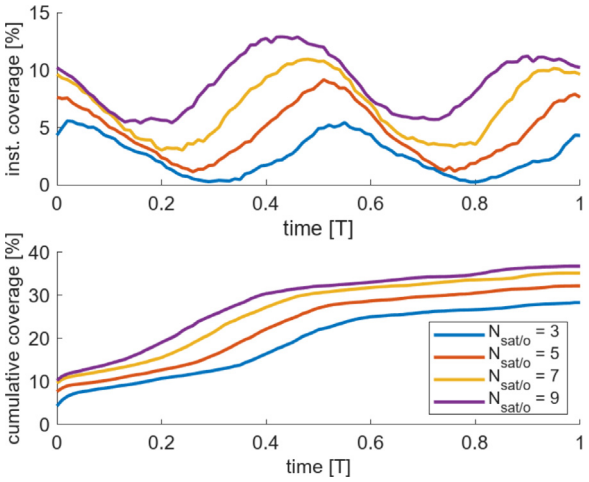


Fig. 28. Performance for varying $N_{sat/o,L}$, overlapped configuration. The time is measured as a fraction of the period T of the constellation.

orbit is enough to have values of cumulative coverage approaching the instantaneous coverage of the complete constellation while retaining an instantaneous coverage of more than 5% every half orbital period. This is an indication that we can reach useable performances with one order of magnitude fewer satellites compared to the optimal constellation obtained in Section 4.2, going from 400 satellites to 45.

To increase the performance, a possibility could be to further reduce the spacing between satellites on the same orbit, increasing the coverage volume along their trajectories. We avoided introducing this design parameter as reducing the spacing too much could cause issues of geometric dilution of precision [33]. Moreover, some care should be used in the interpretation of the simulation results: due to the discrete nature of the vector of time steps used for orbital propagation, the estimated cumulative coverage only accounts for a subset of the continuous coverage volume, therefore resulting in a coverage underestimation of about 1%–2% with a time vector of size $N_t = 200$.

The resulting constellation of 45 satellites divided in batches of three across 15 orbits in an overlapped configuration is capable of delivering about 28% cumulative coverage. This result is strictly tied to the mission objective of observing targets of sizes of 10 cm or more. Requiring only the observation of targets of size greater than 1 m greatly increases the maximum observable distance as shown in Fig. 6, reducing the number of required satellites as a result. This, while not investigated in this paper, opens a path for researching scalable systems that can employ at first only a few satellites for testing surveillance capabilities for large targets. In such a scenario useful results can be obtained long before completing the constellation, thereby increasing the return on the investment and reducing the overall associated risks.

4.6. Extension to other mission objectives

As we explained at the beginning of Section 3, the goal of the constellation design process was to observe targets of size 10 cm over the LEO region. We selected this target size as a reference one for computing the maximum observable distance as in Section 2.2. In reality we may want to maximise the coverage not only over the target population of 10 cm size, but also to consider targets that are bigger than 10 cm. This case is less conservative, as the maximum observable distance increases with the target size as shown in Fig. 6. To compute the coverage over the target population with sizes equal or greater than 10 cm, we can use a Monte Carlo integration as explained in Section 3.4.

In this case, however, the target size should also be sampled using the target distribution in LEO as a function of the target size shown

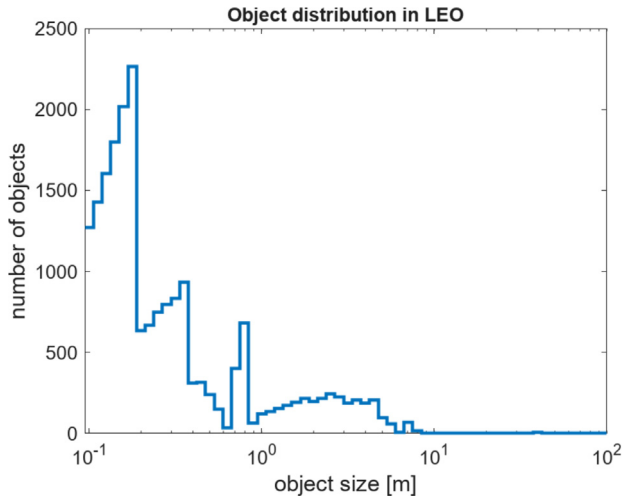


Fig. 29. Target size distribution in LEO as simulated using the ESA Master Software [34]. The *y*-axis indicates the number of objects per size bin. Notice that the *x*-axis is in logarithmic scale.

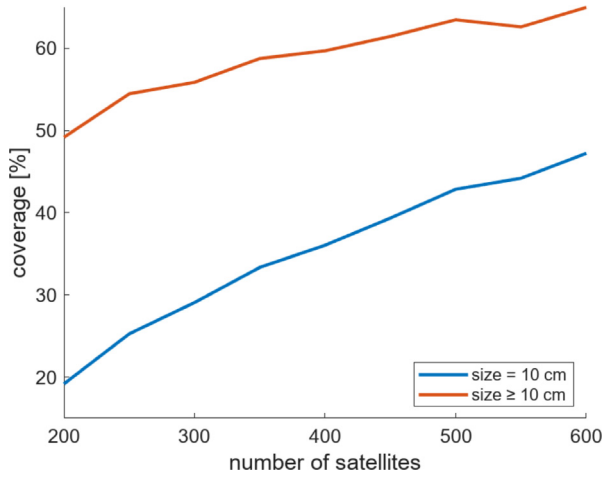


Fig. 30. Triple coverage as a function of the number of constellation satellites. The blue curve considers coverage computed considering only 10 cm targets. The orange curve considers the whole population of size equal or greater than 10 cm. Both cases consider constellation parameters $(N_{sat/o},\ h,\ i,\ \Omega_0,\ \Delta\theta) = (50,\ 460\ \text{km},\ 70°,\ 0°,\ 5°)$ with variable N_o.

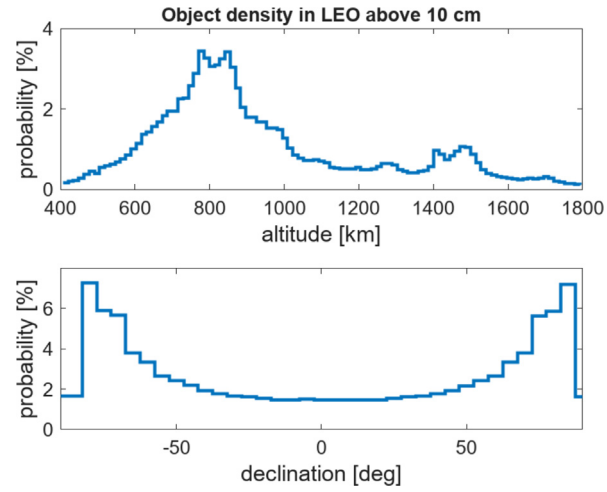


Fig. 31. Target distribution over the LEO region as simulated using the ESA Master Software [34]. The *y*-axis indicates the probability that a target is in the corresponding altitude or declination bin. This distribution considers targets of size 10 cm or higher.

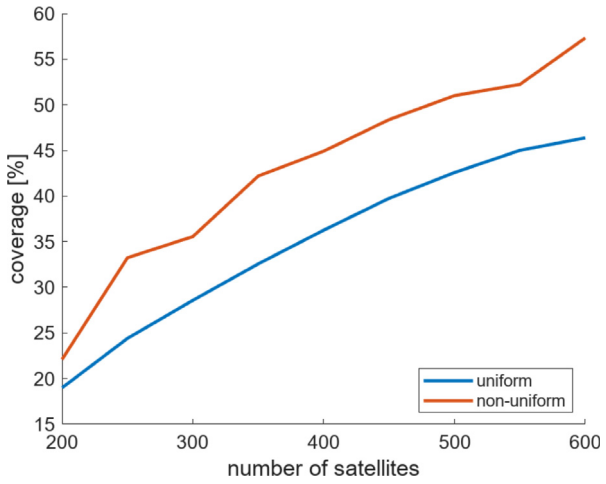


Fig. 32. Triple coverage as a function of the number of constellation satellites. The blue curve considers a uniform target distribution over the LEO region, while the orange one considers the ESA Master estimate shown in Fig. 31. Both cases consider constellation parameters $(N_{sat/o},\ h,\ i,\ \Omega_0,\ \Delta\theta) = (50,\ 460\ \text{km},\ 70°,\ 0°,\ 5°)$ with variable N_o.

in Fig. 29. To quantify the difference between the two cases, we test a constellation with parameters $(N_{sat/o},\ h,\ i,\ \Omega_0,\ \Delta\theta) = (50,\ 460\ \text{km},\ 70°,\ 0°,\ 5°)$ and variable N_o, following the definitions of Table 4. The results are shown in Fig. 30, where we can clearly observe that the case of considering only 10 cm targets is an underestimation of the coverage over the whole population.

The case of considering a non-uniform target distribution over the LEO shell represents another point of discussion not addressed in the main analysis. As explained at the beginning of Section 3, we considered the targets uniformly distributed over the LEO region. This allowed to design a constellation that is not tailored to any specific target distribution, a choice justified by the fact that the target distribution could change in the future. In reality, however, such changes may be very slow. It can therefore make sense to design the constellation using the current population distribution. Fig. 31 shows for instance an estimate of the 2024 population distribution using the ESA Master Software [34], which neglects large constellations that were launched in the past eight years. Using Monte Carlo integration with non-uniform sampling, constellation parameters $(N_{sat/o},\ h,\ i,\ \Omega_0,\ \Delta\theta) = (50,\ 460\ \text{km},\ 70°,\ 0°,\ 5°)$ and variable N_o, we retrieve the two coverage curves in Fig. 32. The results show that not considering the current distribution leads to an underestimation of the coverage of about 10%–20%, but the qualitative behaviour as a function of the constellation satellites is similar.

5. Conclusions

In this paper, we developed methods for the preliminary analysis and design of a space surveillance system comprised of a constellation of satellites carrying optical sensors. Using semi-analytical models for the optical signal-to-noise ratio and the target–observer relative velocity we showed how to decouple the sensor and constellation geometry design problems. Using the resulting estimate for the maximum observable distance and a Monte Carlo integration method, we showed through simulations that daily and yearly variations in coverage are negligible when looking at the average performance. Using random search, we retrieved in a large constellation scenario the optimal Walker-Delta parameters maximising the average coverage, showing that most of the measurement opportunities are concentrated

at high declination values. We proved through simulations that such a constellation would be robust to random satellite loss and to the choice of deployment strategy. Finally, we retrieved an effective architecture for small constellations maximising cumulative coverage. The final design point is a constellation of 45 satellites that exploits field-of-regard overlapping at the poles to achieve 28% cumulative coverage for targets up to 10 cm.

Our research managed to analyse the main performance drivers in distributed space-based surveillance system design and retrieved the optimal parameters of a Walker-Delta constellation together with a global coverage estimate. However, these results stemmed from many simplifying assumptions, including short-distance linearisation for the target velocity, maximum range equal for all target–observer pairs, uniform population distribution over the spherical LEO shell, Keplerian dynamics for the constellation, constant instantaneous coverage. These assumptions are valid in the limiting case of very large constellations and compatible with the 1% Monte Carlo error but should be approached with care when dealing with the fine-tuning of any given design. Moreover, the assumption of a Walker-Delta architecture, albeit compatible with the requirement of a system agnostic to the target population that can be described by a limited number of parameters, constrained the search space to a very limited subset of geometries, potentially neglecting some more effective ones.

Future research could address some of these limitations. Monte Carlo integration could be easily extended to non-uniform populations as shown in Section 4.6. Provided a larger amount of computational resources, a target population of varying size could be simulated directly and the constellation tested for metrics such as the average revisit time or its underlying distribution. This approach could discover interesting interplay between the constellation and target object dynamics as these indeed do not move at random within the shell but are constrained by gravitational dynamics. Discarding the Keplerian dynamics assumption could pave the way to some effective designs that are less expensive in terms of station-keeping manoeuvres: a Sun-synchronous orbit, for instance, would benefit from a more stable yearly coverage and from partial synchronicity with the population of Sun-synchronous satellites. With more computational power, a much larger set of geometries could be explored: a multi-layered constellation could operate effectively at multiple altitudes while minimising field-of-regard overlapping. Moreover, a good system could be sized to optimise scalability for effectively observing progressively smaller targets.

One last issue concerns sustainability. We opened the paper maintaining that a space-based surveillance system could enhance ground-based systems increasing measurement accuracy and availability, ultimately improving the prediction of close approaches and globally reducing collision risk. This, however, comes at a cost that is not just monetary: space-based systems used for collision risk mitigation inject into space for their mere existence additional collision risk. Any spacecraft could collide with the satellites of the constellation, generating debris and disrupting its operations. This is an instance of the space sustainability paradox [35], the condition of being incapable of improving space sustainability without harming it at the same time. Our approach for risk mitigation was to follow the new ESA guidelines for safe space [28] and choose an altitude limiting the lifetime of the constellation satellites to five years. This is however not enough for neglecting the sustainability costs. A better method would be to weigh what are the benefits in terms of reduced risk, computed for instance as a global reduction in the probability of collisions given no collisions with the constellation, against the sustainability costs in terms of added risks, computed for instance as the increase in the probability of collision when the surveillance system is in place assuming no benefits. Such a daunting task would require many assumptions and accurate long-term forecasting of the whole LEO environment, something outside the scope of this work and difficult to do accurately with current methods without large-scale computing. The difficulty of the task together with its importance in cost–benefit analyses warrants further attention in the research community to avoid proposing alleged solutions that could harm the long-term usability of space.

CRediT authorship contribution statement

A. D'Anniballe: Writing – original draft, Visualization, Validation, Software, Methodology, Investigation, Formal analysis, Data curation, Conceptualization. **L. Felicetti:** Writing – review & editing, Supervision, Software, Resources, Methodology, Investigation, Conceptualization. **S. Hobbs:** Writing – review & editing, Supervision.

Declaration of competing interest

The authors declare that they have no known competing financial interests or personal relationships that could have appeared to influence the work reported in this paper.

References

[1] ESA, Annual space environment report, 2023, URL https://www.esa.int/Space_Safety/ESA_s_Space_Environment_Report_2023.

[2] E. Howell, T. Pultarova, Starlink satellites: Facts, tracking and impact on astronomy, 2024, URL https://www.space.com/spacex-starlink-satellites.html.

[3] K. Afifi-Sabet, Project Kuiper: Amazon's answer to SpaceX's Starlink passes 'crucial' test, 2023, URL https://www.space.com/project-kuiper-passes-crucial-test.

[4] A. Jones, The coming Chinese megaconstellation revolution, 2023, URL https://spacenews.com/the-coming-chinese-megaconstellation-revolution/.

[5] B. Weeden, 2007 Chinese anti-satellite test fact sheet, 2010, URL https://swfound.org/media/9550/chinese_asat_fact_sheet_updated_2012.pdf.

[6] B. Weeden, 2009 iridium-cosmos collision fact sheet, 2010, URL https://swfound.org/media/205392/swf_iridium_cosmos_collision_fact_sheet_updated_2012.pdf.

[7] J.E. David, C. Byvik, What's up there, where is it, and what's it doing? The U.S. space surveillance network, 2023, URL https://nsarchive.gwu.edu/briefing-book/intelligence/2023-03-13/whats-there-where-it-and-whats-it-doing-us-space-surveillance.

[8] R. Peldszus, P. Faucher, European union space surveillance & tracking (EU SST): State of play and perspectives, Space Policy (2022) http://dx.doi.org/10.1016/j.spacepol.2022.101503.

[9] I. Molotov, et al., Ison network tracking of space debris: Current status and achievements, in: Revista Mexicana de Astronomía y Astrofísica Serie de Conferencias, 2019, http://dx.doi.org/10.22201/ia.14052059p.2019.51.25.

[10] B. Reihs, et al., Increasing capabilities in a growing radar network, 2022, URL https://amostech.com/TechnicalPapers/2022/SSA-SDA/Reihs.pdf.

[11] C. Liebe, Star trackers for attitude determination, IEEE Aerosp. Electron. Syst. Mag. (1995) http://dx.doi.org/10.1109/62.387971.

[12] eoPortal, Sapphire (space surveillance), 2012, URL https://www.eoportal.org/satellite-missions/sapphire-space-surveillance.

[13] eoPortal, SBSS (space-based surveillance system), 2012, URL https://www.eoportal.org/satellite-missions/sbss.

[14] L. Rider, Optimal orbital constellations for global viewing of targets against a space background, Opt. Eng., Bellingham (1980) http://dx.doi.org/10.1117/12.7972496.

[15] L. Rider, Design of low to medium altitude surveillance systems providing continuous multiple above-the-horizon viewing, Opt. Eng., Bellingham (1989) http://dx.doi.org/10.1117/12.7976896.

[16] K.F. Hussain, K. Thangavel, A. Gardi, R. Sabatini, Autonomous optical sensing for space-based space surveillance, in: 2023 IEEE Aerospace Conference, 2023, http://dx.doi.org/10.1109/AERO55745.2023.10115786.

[17] A.D. Biria, B.G. Marchand, Constellation design for space-based space situational awareness applications: An analytical approach, J. Spacecr. Rockets (2014) http://dx.doi.org/10.2514/1.A32622.

[18] A.T. Takano, B.G. Marchand, AAS 11-543 Optimal constellation design for space based situational awareness applications, 2011, URL https://api.semanticscholar.org/CorpusID:162175545.

[19] Y. Sun, C. Wen, C. Zhang, Z. Zhu, Z. Ye, Above-the-horizon coverage for satellite constellations with dual-altitude band constraints using ring-based discretization, J. Spacecr. Rockets (2022) http://dx.doi.org/10.2514/1.a35333.

[20] A. D'Anniballe, et al., Optimal orbital configurations of spaceborne optical sensors constellations for space surveillance, 2023, URL https://dl.iafastro.directory/event/IAC-2023/paper/79933/.

[21] D.J. Pineau, L. Felicetti, Design of an optical system for a Multi-CubeSats debris surveillance mission, Acta Astronaut. (2023) http://dx.doi.org/10.1016/j.actaastro.2023.04.027.

[22] D.J. Kessler, K.S. Jarvis, Obtaining the properly weighted average albedo of orbital debris from optical and radar data, Adv. Space Res. (2002).

[23] S. Clemens, On-Orbit Resident Space Object (RSO) Detection using commercial grade Star Trackers (Ph.D. thesis), York University, 2019.
[24] H. Curtis, Orbital mechanics for engineering students, 2005, (Chapter 7.2).
[25] C. Xue, H. Cai, S. Gehly, M. Jah, J. Zhang, Review of sensor tasking methods in space situational awareness, Prog. Aerosp. Sci. (2024) http://dx.doi.org/10.1016/j.paerosci.2024.101017.
[26] P. Jiang, C. Liu, W. Yang, Z. Kang, C. Fan, Z. Li, Automatic extraction channel of space debris based on wide-field surveillance system, NPJ Microgravity (2022) http://dx.doi.org/10.1038/s41526-022-00200-z.
[27] J.R. Wertz, Orbit & constellation design & management, 2009, (Chapter 13.2).
[28] ESA, Space debris mitigation requirements, 2023, URL https://sdup.esoc.esa.int/.
[29] ECSS, ECSS-E-ST-10-04C – Space environment, 2008, URL https://ecss.nl/standard/ecss-e-st-10-04c-space-environment/.
[30] ESA, DRAMA, URL https://sdup.esoc.esa.int/.
[31] C.P. Robert, G. Casella, Monte Carlo statistical methods, 2004, (Chapter 3.2).
[32] J. Walker, Satellite constellations, J. Br. Interplanet. Soc. (1984).
[33] R.B. Langley, Dilution of precision, GPS World (1999).
[34] ESA, MASTER, URL https://sdup.esoc.esa.int/.
[35] A.R. Wilson, M. Vasile, The space sustainability paradox, J. Clean. Prod. (2023) http://dx.doi.org/10.1016/j.jclepro.2023.138869.



https://dspace.org/

Preliminary analysis and design of an optical space surveillance and tracking constellation for LEO coverage

D'Anniballe, Antonio; Felicetti, Leonard; Hobbs, Stephen E.

2025-06
Elsevier
https://doi.org/10.1016/j.actaastro.2025.02.019
D'Anniballe A, Felicetti L, Hobbs S. (2025) Preliminary analysis and design of an optical space surveillance and tracking constellation for LEO coverage. Acta Astronautica, Volume 231, June 2025, pp. 47-63

Downloaded from a DSpace repository. https://dspace.org/